Rupture evolution of the 2006 Java tsunami earthquake and the possible role of splay faults

Wenyuan Fan[a,b], Dan Bassett[a,c], Junle Jiang[a], Peter M. Shearer[a], Chen Ji[d,e]

[a] *Scripps Institution of Oceanography, UC San Diego, La Jolla, CA 92093-0225, USA.*
[b] *Woods Hole Oceanographic Insitution, Woods Hole, MA 02543, USA.*
[c] *GNS Science, Lower Hutt, 5010, New Zealand.*
[d] *Earth Research Institute, UC, Santa Barbara, Santa Barbara, CA 93106, USA.*
[e] *Department of Earth Science, UC, Santa Barbara, Santa Barbara, CA 93106, USA.*

Abstract

The 2006 Mw 7.8 Java earthquake was a tsunami earthquake, exhibiting frequency-dependent seismic radiation along strike. High-frequency global back-projection results suggest two distinct rupture stages. The first stage lasted ∼65 s with a rupture speed of ∼1.2 km/s, while the second stage lasted from ∼65 to 150 s with a rupture speed of ∼2.7 km/s. High-frequency radiators resolved with back-projection during the second stage spatially correlate with splay fault traces mapped from residual free-air gravity anomalies. These splay faults also colocate with a major tsunami source associated with the earthquake inferred from tsunami first-crest back-propagation simulation. These correlations suggest that the splay faults may have been reactivated during the Java earthquake, as has been proposed for other tsunamigenic earthquakes, such as the 1944 Mw 8.1 Tonankai earthquake in the Nankai Trough.

Keywords: Earthquake, Tsunami, Back-projection, Splay faults, Java, Seismology

1. Introduction

Tsunami earthquakes are characterized by a disproportionately large tsunami for their size, and often exhibit a disparity between estimates of moment magnitude derived from long and short period seismic radiation (*Kanamori*, 1972; *Kanamori and Kikuchi*, 1993). The July 17, 2006 Java earthquake was a classic tsunami earthquake with body-wave magnitude mb = 6.1, surface-wave magnitude Ms = 7.1, and moment magnitude Mw = 7.7 (*International Seismological Centre*, 2013; *Ekström et al.*, 2012). Such a large variation in magnitude estimates is atypical and may indicate a deficiency in high-frequency radiation compared to low-frequency radiation (*Newman and Okal*, 1998; *Ammon et al.*, 2006). The 2006 Java earthquake initiated at shallow depth (20 km, (*International Seismological Centre*, 2013); Figure 1) and ruptured eastward along the trench axis for ∼200 km (*Ammon et al.*, 2006; *Bilek and Engdahl*, 2007). Given the source dimension, the unusually long source duration (∼185 s) indicates anomalously slow rupture propagation for the event (*Ammon et al.*, 2006; *Bilek and Engdahl*, 2007). The earthquake generated a large tsunami (∼8 m) resulting in over 800 fatalities (*Fritz et al.*, 2007; *Fujii and Satake*, 2006; *Mori et al.*, 2007). This was the second tsunami earthquake that struck the Java region since instrumental records began, and a Mw 7.8 earthquake in June 1994 produced an even larger tsunami (∼13 m), resulting in 250 fatalities (*Abercrombie et al.*, 2001; *Mori et al.*, 2007). These two earthquakes are only 600 km apart, highlighting the major tsunami hazard along the south coast of Indonesia (*Mori et al.*, 2007). Is the Java trench prone to more tsunami earthquakes and if so, what properties of the margin promote this type of rupture?

Finite-fault slip models of the 2006 Java earthquake suggest a smooth slip distribution with an unusually slow (∼1 km/s) rupture propagation (Figure 2b). Finite-fault slip models obtained from body waves (P and SH waves, ∼0.001–0.2 Hz) have similar slip distributions, with the largest slip concentrated near the hypocenter (Figure 2b) (*Ammon et al.*, 2006; *Bilek and Engdahl*, 2007; *Yagi and Fukahata*, 2011; *Ye et al.*, 2016a,b). In contrast, finite-fault slip models obtained from both body and surface waves (both Rayleigh and Love waves) suggest the largest slip is close to the trench and is up-dip and ∼50 km east of the hypocenter (Figure 2) (*Hayes*, 2011; *Shao et al.*, 2011). Surface waves have been shown to be effective at resolving near-trench slip distributions, which are difficult to resolve just with body waves (*Shao et al.*, 2011).

The 2006 Java earthquake was one of the best-recorded tsunami earthquakes with modern instruments. Combining the wealth of data with new observational approaches enables us to investigate the earthquake in great detail. We first analyze bathymetry and gravity anomalies in conjunction with active-source seismic profiles to constrain margin structure and the location of splay faults. We then build on published kinematic slip models of the 2006 Java earthquake source by performing global P-wave back-projection using two different frequency bands to examine the earthquake kinematics. In addition, we back-propagate first-crest arrivals in tsunami waveforms of five nearby tide gauges at various azimuths to locate tsunami sources. Our high-frequency back-projection results suggest a unilateral rupture extending ∼200 km with a slow first-stage rupture (∼1.2 km/s) from west to east until ∼65 s and a fast second-stage rupture (∼ 2.7 km/s) from ∼65 to 150 s.

The second-stage rupture colocates with a major tsunami source located by first-crest tsunami back-propagation. The spatial correlation between the stage-two rupture imaged by back-projection and splay fault traces delineated by gravity data suggests that splay faults may have been reactivated during the 2006 Java earthquake and possibly contributed to tsunamigenesis. This mechanism of enhanced tsunami excitation due to splay faulting has been proposed for the 1944 Mw 8.1 Tonankai earthquake in the Nankai Trough (*Moore et al.*, 2007).

2. Tectonic Setting and Residual Gravity Anomaly

The Java subduction zone accommodates underthrusting of the Indo-Australian plate beneath Eurasia at approximately 67 mm/yr (*Tregoning et al.*, 1994). The incoming plate in offshore western Java is structurally complex, hosting a dense population of seamounts and the Roo Rise oceanic plateau (*Shulgin et al.*, 2011). The forearc is characterized by an outer-arc high, which typically extends 100 km from the trench-axis with water-depths of 2-3 km (*Kopp et al.*, 2002; *Planert et al.*, 2010). Landward of the outer-arc high, the Lombok forearc basin extends along the coastline of Java for over 400 km.

Short wavelength topographic and gravimetric anomalies can illuminate detailed structure of the overthrusting and subducting plates. These short wavelength features can be effectively extracted using spectral averaging methods designed specifically to suppress steep topographic and gravimetric gradients across subduction zones (*Bassett and Watts*, 2015a,b). Application of these methods to the Java subduction zone reveals a long array of lineations

in the residual gravity field, encompassing the full ∼100 km trench-normal width of the outer-arc high and the full ∼ 800 km along-strike extent of the Java margin (Arrows, Figure 1). Where 2D seismic reflection and refraction profiles traverse the forearc (Red line, Figure 1), the gravity lineations are consistent with the locations of splay faults imaged in the overthrusting plate (*Kopp et al.*, 2009). The lateral continuity of the residual gravity field allows us to extend this interpretation along strike, which indicates that the outer-arc high is pervasively faulted and that splay faults are almost certainly present within the source region of the 1994 and 2006 tsunami earthquakes (Figure 1).

3. Seismic P-wave Back-projection

We perform P-wave back-projection using the procedure described in *Fan and Shearer* (2015), using vertical-component velocity records from the International Federation of Digital Seismograph Networks (FDSN) seismic stations that are available and distributed by the Data Management Center (DMC) of the Incorporated Research Institutions for Seismology (IRIS). Because back-projection techniques do not make assumptions about fault geometry or rupture velocity, they are able to resolve complex earthquake behavior, such as variable rupture velocity, multiple events, and very early aftershocks (*Ishii et al.*, 2005; *Xu et al.*, 2009; *Koper et al.*, 2011; *Kiser and Ishii*, 2011; *Meng et al.*, 2012; *Satriano et al.*, 2012; *Nissen et al.*, 2016; *Wang et al.*, 2016). Global back-projection is particularly effective in detecting frequency-dependent radiation because of its superior spatial resolution (e.g., *Walker et al.*, 2005; *Yagi et al.*, 2012; *Okuwaki et al.*, 2014).

In practice, P-wave velocity seismograms are initially filtered into two frequency bands, a high-frequency (HF) band (0.3-1 Hz) and a low-frequency (LF) band (0.05-0.3 Hz), to examine potential frequency-dependent seismic radiation. Second, the filtered data are then visually inspected, and only traces with clear initial P-wave arrivals are kept. For robustness, stations with theoretical negative lower-hemisphere polarities are removed based on the GCMT solution of the earthquake (*Ekström et al.*, 2012). Third, we divide the Earth's surface into 1° by 1° azimuthal-epicentral-distance cells where the epicenter is at the center. Within each cell, traces are then aligned with cross-correlation, and only the station with the highest cross-correlation coefficient is kept per cell. Fourth, the traces extracted from each cell (68 stations) are aligned by cross-correlating the initial few seconds of P-waves separately at the two frequency bands (*Houser et al.*, 2008). The cross-correlating windows are from -3 s to 4 s and -1 s to 4 s for the low- and high-frequency bands based on the IASP91 model (*Kennett and Engdahl*, 1991), allowing maximum time shifts of 5 s and 4 s for the two frequency bands respectively. The alignment is applied to neutralize the influence of 3D velocity structure. No polarity flips are allowed during the alignment. (Figure S2). We then set up the potential sources gridded at 10-km horizontal spacing, fixed at the hypocentral depth (20 km). The grid latitudes range from $-12°$ to $-6.6°$, and grid longitudes range from 105.5° to 111.1° (600 km by 600 km). Finally, back-projection is performed with Nth root stacking ($N = 4$), which can improve spatial resolution of back-projection images at the cost of losing absolute amplitude information (*Rost and Thomas*, 2002; *Xu et al.*, 2009) (Figure 3). When performing back-projection, the records are normalized,

weighted by their average correlation coefficients obtained from the cross-correlation alignment, and inversely scaled by the number of contributing stations within 5 degrees, which downweights the noisy records and prevents over-representation of data from dense local arrays. We obtain a peak-power time function with a non-overlapping 2 s window that is the maximum back-projected power of the potential sources (location of high-frequency bursts) (*Kiser and Ishii*, 2013; *Fan and Shearer*, 2016). The back-projection snapshots are computed with 20-s stacking windows and are normalized by the maximum power within each window (Figure 2, 3). The robustness of the resolved snapshots is assessed by jackknife resampling (*Efron and Tibshirani*, 1994; *Fan and Shearer*, 2016) and we reject snapshots with peak-power spatial standard errors greater than 0.5° for either latitude or longitude (∼ 50 km). No post-processing is applied to the final images.

Our back-projection peak-power time functions agree with prior studies that indicate the 2006 Java earthquake had an abnormally long duration. The LF peak-power time function suggests it lasted ∼180 s, which is consistent with long-period finite-fault modeling (e.g., *Ammon et al.*, 2006), while the HF peak-power time function indicates at least ∼150 s of continuous seismic radiation (Figure 2a). Stacked envelope functions (1-5 Hz) with globally distributed stations also suggest a very long rupture duration lasting ∼150 s (Figure S3).

In the first 60 s, both LF and HF back-projection results show similar seismic radiation (Figure 3). The time-integrated back-projection image (Figure 3a,c) suggests that the bulk of seismic radiation was excited around the epicenter during the early phase of the earthquake (Figure 3b,d). Af-

ter 60 s, the back-projection snapshots indicate frequency-dependent seismic radiation (Figure 3). HF back-projection snapshots show west-to-east linear rupture propagation from 60 to 160 s. The 100–120 s LF back-projection snapshot seems to correspond to the overall rupture propagation (Figure 2b,3a) because its location and average rupture speed agree with the expected rupture propagation (∼1 km/s), while the 120–180 s LF back-projection snapshots are significantly down-dip of the mainshock epicenter (∼70 to ∼170 km), suggesting possible nearby triggered early aftershocks (*Fan and Shearer*, 2016). Finite-fault models have limited resolution for the later stage of the mainshock rupture, suggested by their discrepancies, showing minor to negligible slip after 140 s (*Ammon et al.*, 2006; *Bilek and Engdahl*, 2007; *Yagi and Fukahata*, 2011; *Ye et al.*, 2016a,b). As shown by globally recorded 0.02–0.05 Hz P-waves, identifiable phases are present from 120 s to 200 s (Figure S5). These phases are coherent in the azimuthal range of the stations used for back-projection, which is likely why back-projection detected those coherent energy bursts. The polarity patterns of these phases are different than those of the mainshock, and the amplitudes vary gradually with azimuth (Figure S5). These phases are unlikely to be water-phases nor part of the mainshock because of the azimuthally dependent radiation pattern. The varying radiation pattern, e.g., polarities, can potentially be used to resolve the focal mechanisms of these possible aftershocks. However, it is challenging to make robust picks, leaving the focal mechanisms yet to be determined with future analysis.

A plot of cumulative rupture distance as a function of time (Figure 4) provides estimates of average rupture speeds. The cumulative distance was

computed from HF back-projection peak-power locations (20 s stacking window with 1 s temporal increment, Figure 2b). The results suggest an increase in rupture velocity around 65 s (Figure 4c). Similar to the rupture speed resolved from finite-fault inversions (e.g., *Ammon et al.*, 2006; *Yagi and Fukahata*, 2011), the first stage ruptured slowly (∼1.2 km/s) for about 65 s, while the second stage ruptured no slower than 2.5 km/s from ∼65 to 150 s, propagating eastward at about 2.7 km/s on average (Figure 4). If the rupture propagation transitioned near 90 s (suggested by an alternative intersection of finite-fault slip models and back-projection inferred rupture velocities), the second stage rupture velocity may be as high as 3.2 km/s. There is no evidence of supershear rupture episodes during the earthquake, suggesting the second stage more likely transitioned at ∼65 s, restrained by the local S-wave velocity (*Kopp et al.*, 2009; *Laske et al.*, 2013). Intriguingly, the HF back-projection snapshots indicate west to east migration in seismic radiation for the second stage of the event (Figure 2b,3d), which spatially correlates with the location of slay fault traces inferred from residual gravity anomalies (Figure 1).

4. Tsunami Tide Gauge Back-propagation

To constrain tsunami source locations, we perform tsunami back-propagation with five nearby tide gauges recording the tsunami of the 2006 Java earthquake (Figure 5a). The tsunami waveforms are high-pass filtered at 2 hours to remove tidal signals, from which the initial and first-crest arrivals are estimated (Table 1). With the first-crest arrivals, back-propagation of tsunami waves from the tide gauges is used to delineate possible source locations of sea

surface displacements (Figure 5b–f). We consider Gaussian-shaped seafloor uplifts as tsunami sources centered at the gauge locations with half-widths of 2 km. Tsunami propagation is computed with nonlinear shallow water-wave equations (*Liu et al.*, 1995) and General Bathymetric Chart of the Oceans (GEBCO) 30 arc-second bathymetry (*Weatherall et al.*, 2015). To account for the long-wave dispersion that is missing in our numerical simulations, the observed first-crest arrivals are shifted 1% earlier for all stations. This shift is derived from comparisons between tsunami models and observations from recent great earthquakes (*Tsai et al.*, 2013; *Watada et al.*, 2014).

Regions bounded by multiple arcs of the back-propagated tsunami first-crest wavefronts indicate the possible tsunami source areas (Figure 6). These tsunami sources were excited by local large seafloor displacements. To account for the uncertainty in tsunami modeling, we identify source regions using the first-wave bands instead of crest lines, which are contours with tsunami amplitudes greater than 50% of the crest (Figure 5,6). The back-propagation results suggest two possible main sources for the observed tsunami (Figure 6). The first source is bounded by two arcs close to the epicenter (from Christmas and Hillarys), and the second source is bounded by four arcs close to the second stage high-frequency seismic radiation (from Benoa, Cocos, Broome, and Hillarys). The second source is more than 100 km eastward of the epicenter. Intriguingly, tsunami back-propagation of the Cocos gauge, west of the 2006 Java earthquake (Figure 5d), only tracks the eastern tsunami source, suggesting that the western source may be weaker than the source located to the east. The tsunami sources we resolve are generally consistent with *Fujii and Satake* (2006), who suggested a major tsunami source

∼150 km east of the epicenter. The eastward source is around the zones of inferred splay faults and correlates with high-frequency radiation from ∼ 60 to 150 s (Figure 6).

5. Discussion

Tsunami waveform inversion suggests that the tsunami source of the 2006 Java earthquake was about 200 km long with the largest slip (∼2.5 m) stably located about 150 km east of the epicenter, regardless of the assumed earthquake rupture velocity (*Fujii and Satake*, 2006). This tsunami-derived slip model is significantly different from the seismic slip models (*Fujii and Satake*, 2006; *Ammon et al.*, 2006; *Bilek and Engdahl*, 2007; *Yagi and Fukahata*, 2011; *Ye et al.*, 2016a), which suggest the largest slip occurred within 50 km of the epicenter. The slip model discrepancies may be attributed to two possibilities: (1), tsunami data and seismic data have different spatial sensitivities over the slip distribution (e.g., *Melgar et al.*, 2016; *Jiang and Simons*, 2016). The eastward tsunami source may have been generated by coseismic slip on the main thrust, which was missed by the seismic finite-fault inversion. (2), Slip at the plate interface is not the only source responsible for the observed tsunami. In this case, more than one fault caused the seafloor displacement and contributed to generating the large tsunami. Possible splay fault activation may explain the observations because of their enhanced tsunamigenic capabilities. Slip on splay faults with steep dipping angles will cause larger seafloor displacement, which drives tsunami generation (*Jiang and Simons*, 2016), than the same amount of slip on the subhorizontal megathrust.

Rupture velocity evolution suggests that the 2006 Java earthquake ra-

diated high-frequency energy in a two-stage fashion, with a transition around 60 s (Figure 4). Stage one was characterized by a rupture velocity of ∼1.2 km/s for about 65 s, and may be deficient in high frequencies comparing to the second stage. In contrast, the stage-two high-frequency radiators migrated from west to east at more than twice the rupture speed observed during stage one (∼ 2.7 km/s). This atypical abrupt two-stage HF energy release may suggest that more than one source generated the high-frequency radiation.

The observations cannot distinguish whether the rupture transition occurred sharply or gradually. The precise HF radiation transition timing is ambiguous, leaving the exact initiation time of the second stage unclear (Figure 4). Nonetheless, the differences in seismic radiation between the two stages are robust. The two-stages of observed rupture may simply reflect rupture complexities along strike, as has been reported for other large earthquakes (e.g., *Kiser and Ishii*, 2011; *Wei et al.*, 2011). Fault geometry, heterogeneous initial stress at the plate interface, or heterogeneous friction properties could all produce along-strike variations of high-frequency radiation (e.g., *Madariaga*, 1977; *Bernard and Madariaga*, 1984; *Spudich and Frazer*, 1984; *Fukahata et al.*, 2014; *Denolle et al.*, 2015; *Bassett et al.*, 2016).

Alternatively, the colocation of the second-stage high-frequency radiators with splay faults and the eastward tsunami source may indicate splay-fault reactivation during the 2006 Java earthquake (Figure 2–5). Active-source seismic profiles 100 km west of the 2006 Java earthquake epicenter resolve steep north-dipping splay faults that are well correlated with their locations inferred by residual gravity anomalies (*Kopp et al.*, 2009). These splay faults extend along the forearc and are present in the vicinity of both the 2006

and 1994 Java tsunami earthquakes (Figure 1). The ISC catalog (1993-2013) locates some shallow seismicity close to the 2006 Java earthquake (59 earthquakes shallower than 10 km and 122 earthquakes at 10 to 20 km), which may provide further evidence of seismic activity along splay faults (Figure 1) (*International Seismological Centre*, 2013). Although back-projection method does not have the depth resolution to discriminate between radiation from the splay faults and from the plate interface, the transition in HF seismic radiation and the strong spatial correlation between the stage-two rupture and the splay fault traces suggest that reactivated splay faults may have been a key source of HF seismic radiation and seafloor displacement during the second-stage rupture (Figure 2–6).

Splay fault activation during the mainshock rupture has been reported for earthquakes in the Nankai, Kuril, Alaska, and Sumatra subduction zones (*Plafker*, 1969, 1972; *Fukao*, 1979; *Moore et al.*, 2007; *DeDontney and Rice*, 2012; *Waldhauser et al.*, 2012). Numerical models have also validated the possibility of splay-fault reactivation during megathrust ruptures (*Wang and He*, 1999; *Kame et al.*, 2003; *Wang and Hu*, 2006; *Wendt et al.*, 2009; *Tamura and Ide*, 2011; *DeDontney and Hubbard*, 2012). At the Nankai trough, the presence of a megasplay fault and evidence for large-scale sediment slumping suggests that splay fault activation may have contributed to tsunamigenesis during the 1944 Mw 8.1 Tonankai earthquake (*Moore et al.*, 2007). Splay fault activation has similarly been proposed for the 1964 Mw 9.2 Alaska earthquake (*Plafker*, 1969, 1972) and the 2004 Mw 9.3 Sumatra-Andaman earthquake (*DeDontney and Rice*, 2012). From analyses of multiple geophysical observations, we suggest a similar scenario may have occurred along

the Java trench, with coseismic splay fault reactivation providing one viable mechanism to explain our observations.

6. Conclusions

The 2006 Mw 7.8 Java earthquake ruptured more than 200 km from west to east, lasting for more than ∼180 s. Finite-fault slip models suggest a smooth and slow rupture with the largest slip patch within ∼50 km away from the hypocenter (*Ammon et al.*, 2006; *Bilek and Engdahl*, 2007; *Yagi and Fukahata*, 2011; *Ye et al.*, 2016a,b), which is supported by our low-frequency back-projection results. In contrast, high-frequency global back-projection results suggest a two-stage rupture. The first stage ruptured with an unusually low rupture speed of ∼1.2 km/s, agreeing well with finite-fault slip models (e.g., *Ammon et al.*, 2006), while the second stage ruptured with a much faster speed of ∼ 2.7 km/s. While the back-projection cannot resolve the depth of the radiators, their spatial correlation with traced and active splay faults and the abrupt change in kinematic signatures during the second stage of the rupture may indicate a jump during the rupture to these splay faults. The hypothesis is further supported by the tsunami first crest arrival back-propagation, which shows that at least two sources contributed to the observed tsunami. The two sources were separated by more than 100 km, with the first source close to the epicenter and the second source spatially correlating with the inferred splay fault traces. The residual gravity anomalies delineate multiple trench-parallel splay faults near both the 1994 and 2006 Java tsunami earthquakes, raising concerns of enhanced tsunami hazard in the region. Similar tsunamigenic earthquakes, such as the 1944 Mw 8.1 To-

nankai earthquake and the 2004 Mw 9.3 Sumatra-Andaman earthquake, have been proposed to also activate splay faults during the rupture propagation, and splay fault networks may play a critical role in enhancing tsunamigenesis during large megathrust earthquakes.

7. Acknowledgments

We thank the editor Dr. Kelin Wang and two reviewers for their constructive suggestions, which led to improvements in our paper. We would also like to thank Lingling Ye for sharing her finite-fault slip model. Finite-fault slip model of *Yagi and Fukahata* (2011) is downloaded from the Source Inversion Validation (SIV) database (SRCMOD, http://equake-rc.info/) (*Mai et al.*, 2016). Finite-fault slip model obtained with both body and surface waves is downloaded from the U.S. Geological Survey National Earthquake Information Center (*Duputel et al.*, 2011; *Hayes*, 2011; *Hayes et al.*, 2011). The facilities of IRIS Data Services, and specifically the IRIS Data Management Center, were used for access to waveforms, related metadata, and/or derived products used in this study. IRIS Data Services are funded through the Seismological Facilities for the Advancement of Geoscience and EarthScope (SAGE) Proposal of the National Science Foundation under Cooperative Agreement EAR-1261681. Tsunami data are provided by the University of Hawaii Sea Level Center and Bureau of Meteorology, Research Centre, Australian Government. The earthquake catalog was downloaded from the International Seismological Center (ISC). The bathymetry and gravity data were processed with the Generic Mapping Tools (GMT) (*Wessel and Smith*, 1991; *Wessel et al.*, 2013). W.F. is currently supported by the Postdoctoral

Scholar Program at the Woods Hole Oceanographic Institution, with funding provided by the Weston Howland Jr. Postdoctoral Scholarship. This work was supported by National Science Foundation grant EAR-1620251 at Scripps Institution of Oceanography, UC San Diego.

References

Abercrombie, R. E., M. Antolik, K. Felzer, and G. Ekström (2001), The 1994 Java tsunami earthquake: Slip over a subducting seamount, *J. Geophys. Res.*, *106*(B4), 6595–6607, doi:10.1029/2000JB900403.

Ammon, C. J., H. Kanamori, T. Lay, and A. A. Velasco (2006), The 17 July 2006 Java tsunami earthquake, *Geophys. Res. Lett.*, *33*(24), doi:10.1029/2006GL028005, l24308.

Bassett, D., D. T. Sandwell, Y. Fialko, and A. B. Watts (2016), Upper–plate controls on co-seismic slip in the 2011 magnitude 9.0 Tohoku-oki earthquake, *Nature*, doi:10.1038/nature16945.

Bassett, D., and A. B. Watts (2015a), Gravity anomalies, crustal structure, and seismicity at subduction zones: 1. Seafloor roughness and subducting relief, *Geochem. Geophys. Geosyst.*, *16*(5), 1508–1540, doi:10.1002/2014GC005684.

Bassett, D., and A. B. Watts (2015b), Gravity anomalies, crustal structure, and seismicity at subduction zones: 2. Interrelationships between fore-arc structure and seismogenic behavior, *Geochem. Geophys. Geosyst.*, *16*(5), 1541–1576, doi:10.1002/2014GC005685.

391 Bernard, P., and R. Madariaga (1984), A new asymptotic method for the
392 modeling of near-field accelerograms, *Bull. Seismol. Soc. Am.*, *74*(2), 539–
393 557.

394 Bilek, S. L., and E. R. Engdahl (2007), Rupture characterization and after-
395 shock relocations for the 1994 and 2006 tsunami earthquakes in the Java
396 subduction zone, *Geophys. Res. Lett.*, *34*(20), doi:10.1029/2007GL031357,
397 l20311.

398 DeDontney, N., and J. Hubbard (2012), Applying wedge theory to dynamic
399 rupture modeling of fault junctions, *Bull. Seismol. Soc. Am.*, *102*(4), 1693–
400 1711, doi:10.1785/0120110190.

401 DeDontney, N., and J. R. Rice (2012), Tsunami wave analysis and possibility
402 of splay fault rupture during the 2004 Indian ocean earthquake, *Pure Appl.*
403 *Geophys.*, *169*(10), 1707–1735, doi:10.1007/s00024-011-0438-4.

404 Denolle, M. A., W. Fan, and P. M. Shearer (2015), Dynamics of the
405 2015 M7.8 Nepal earthquake,*Geophys. Res. Lett.42*(18), 7467–7475, doi:
406 10.1002/2015GL065336, 2015GL065336.

407 Duputel, Z., L. Rivera, H. Kanamori, G. P. Hayes, B. Hirshorn, and S. Wein-
408 stein (2011), Real-time W–phase inversion during the 2011 off the Pacific
409 coast of Tohoku earthquake, *Earth, Planets, Space*, *63*(7), 535–539, doi:
410 10.5047/eps.2011.05.032.

411 Efron, B., and R. J. Tibshirani (1994), *An introduction to the bootstrap*, CRC
412 Press.

Ekström, G., M. Nettles, and A. Dziewoński (2012), The global CMT project 2004–2010: Centroid-moment tensors for 13,017 earthquakes, *Phys. Earth Planet. Inter.*, *200–201*(0), 1–9, doi: http://dx.doi.org/10.1016/j.pepi.2012.04.002.

Fan, W., and P. Shearer (2015), Detailed rupture imaging of the 25 April 2015 Nepal earthquake using teleseismic P waves, *Geophys. Res. Lett.42*(14), 5744–5752, doi:10.1002/2015GL064587, 2015GL064587.

Fan, W., and P. M. Shearer (2016), Local near instantaneously dynamically triggered aftershocks of large earthquakes, *Science*, *353*(6304), 1133–1136, doi:10.1126/science.aag0013.

Fritz, H. M., W. Kongko, A. Moore, B. McAdoo, J. Goff, C. Harbitz, B. Uslu, N. Kalligeris, D. Suteja, K. Kalsum, V. Titov, A. Gusman, H. Latief, E. Santoso, S. Sujoko, D. Djulkarnaen, H. Sunendar, and C. Synolakis (2007), Extreme runup from the 17 July 2006 Java tsunami, *Geophys. Res. Lett.*, *34*(12), doi:10.1029/2007GL029404, l12602.

Fujii, Y., and K. Satake (2006), Source of the July 2006 west Java tsunami estimated from tide gauge records, *Geophys. Res. Lett.*, *33*(24), doi: 10.1029/2006GL028049, l24317.

Fukahata, Y., Y. Yagi, and L. Rivera (2014), Theoretical relationship between back-projection imaging and classical linear inverse solutions, *Geophys. J. Int.*, *196*(1), 552–559.

Fukao, Y. (1979), Tsunami earthquakes and subduction processes

near deep-sea trenches, *J. Geophys. Res.*, *84*(B5), 2303–2314, doi: 10.1029/JB084iB05p02303.

Garcia, E. S., D. T. Sandwell, and W. H. Smith (2014), Retracking Cryosat-2, Envisat and Jason-1 radar altimetry waveforms for improved gravity field recovery, *Geophys. J. Int.*, *196*(3), 1402–1422, doi:10.1093/gji/ggt469.

Hayes, G. P. (2011), Rapid source characterization of the 2011 Mw 9.0 off the Pacific coast of Tohoku earthquake, *Earth, Planets, Space*, *63*(7), 529–534, doi:10.5047/eps.2011.05.012.

Hayes, G. P., P. S. Earle, H. M. Benz, D. J. Wald, R. W. Briggs, and the USGS/NEIC Earthquake Response Team (2011), 88 hours: The U.S. Geological Survey National Earthquake Information Center response to the 11 March 2011 Mw 9.0 Tohoku earthquake, *Seismol. Res. Lett.*, *82*(4), 481–493, doi:10.1785/gssrl.82.4.481.

Hayes, G. P., D. J. Wald, and R. L. Johnson (2012), Slab1.0: A three-dimensional model of global subduction zone geometries, *J. geophys. Res.117*(B1), doi:10.1029/2011JB008524, b01302.

Houser, C., G. Masters, P. Shearer, and G. Laske (2008), Shear and compressional velocity models of the mantle from cluster analysis of long-period waveforms, *Geophys. J. Int.*, *174*(1), 195–212, doi:10.1111/j.1365-246X.2008.03763.x.

International Seismological Centre (2013), *On-line Bulletin*, Int. Seis. Cent., Thatcham, United Kingdom (2013).

457 Ishii, M., P. M. Shearer, H. Houston, and J. E. Vidale (2005), Extent, dura-
458 tion and speed of the 2004 Sumatra-Andaman earthquake imaged by the
459 Hi-net array, *Nature*, *435*(7044), 933–936.

460 Laske, G., G. Masters, Z. Ma, and M. Pasyanos (2013), Update on
461 CRUST1.0-A 1-degree global model of Earths crust, in *Geophys. Res. Ab-*
462 *stracts*, vol. 15, p. 2658.

463 Jiang, J., and M. Simons (2016), Probabilistic imaging of tsunamigenic
464 seafloor deformation during the 2011 Tohoku-Oki earthquake, *J. geophys.*
465 *Res.121*(12), 9050–9076, doi:10.1002/2016JB013760, 2016JB013760.

466 Kame, N., J. R. Rice, and R. Dmowska (2003), Effects of prestress state and
467 rupture velocity on dynamic fault branching, *J. geophys. Res.108*(B5),
468 doi:10.1029/2002JB002189, 2265.

469 Kanamori, H. (1972), Mechanism of tsunami earthquakes, *Phys.*
470 *Earth Planet. Inter.*, *6*(5), 346–359, doi:http://dx.doi.org/10.1016/0031-
471 9201(72)90058-1.

472 Kanamori, H., and M. Kikuchi (1993), The 1992 Nicaragua earthquake: a
473 slow tsunami earthquake, *Nature*, *361*, 25.

474 Kennett, B. L. N., and E. R. Engdahl (1991), Traveltimes for global earth-
475 quake location and phase identification, *Geophys. J. Int.*, *105*(2), 429–465,
476 doi:10.1111/j.1365-246X.1991.tb06724.x.

477 Kiser, E., and M. Ishii (2011), The 2010 Mw 8.8 Chile earthquake: Triggering
478 on multiple segments and frequency-dependent rupture behavior, *Geophys.*
479 *Res. Lett.38*(7), doi:10.1029/2011GL047140, l07301.

480 Kiser, E., and M. Ishii (2013), Hidden aftershocks of the 2011 Mw 9.0 Tohoku,
481 Japan earthquake imaged with the backprojection method, *J. Geophys.*
482 *Res.*, *118*(10), 5564–5576, doi:10.1002/2013JB010158, 2013JB010158.

483 Koper, K. D., A. H. T. Lay, C. Ammon, and H. Kanamori (2011), Frequency-
484 dependent rupture process of the 2011 Mw 9.0 Tohoku earthquake: Com-
485 parison of short-period P wave backprojection images and broadband seis-
486 mic rupture models, *Earth, Planets, Space*, *63*(7), 599.

487 Kopp, H., D. Klaeschen, E. R. Flueh, J. Bialas, and C. Reichert (2002),
488 Crustal structure of the Java margin from seismic wide-angle and mul-
489 tichannel reflection data, *J. geophys. Res.107*(B2), ETG 1–1–ETG 1–24,
490 doi:10.1029/2000JB000095.

491 Kopp, H., D. Hindle, D. Klaeschen, O. Oncken, C. Reichert, and D. Scholl
492 (2009), Anatomy of the western Java plate interface from depth-
493 migrated seismic images, *Earth Planet. Sci. Lett.*, *288*(3-4), 399–407, doi:
494 http://dx.doi.org/10.1016/j.epsl.2009.09.043.

495 Liu, P. L. F., Y. S. Cho, S. B. Yoon, and S. N. Seo (1995), *Numerical Simu-*
496 *lations of the 1960 Chilean Tsunami Propagation and Inundation at Hilo,*
497 *Hawaii*, pp. 99–115, Springer Netherlands, Dordrecht, doi:10.1007/978-94-
498 015-8565-1_7.

499 Madariaga, R. (1977), High-frequency radiation from crack (stress drop)
500 models of earthquake faulting, *Geophys. J. Int.*, *51*(3), 625–651, doi:
501 10.1111/j.1365-246X.1977.tb04211.x.

Mai, P. M., D. Schorlemmer, M. Page, J.-P. Ampuero, K. Asano, M. Causse, S. Custodio, W. Fan, G. Festa, M. Galis, F. Gallovic, W. Imperatori, M. Käser, D. Malytskyy, R. Okuwaki, F. Pollitz, L. Passone, H. N. T. Razafindrakoto, H. Sekiguchi, S. G. Song, S. N. Somala, K. K. S. Thingbaijam, C. Twardzik, M. van Driel, J. C. Vyas, R. Wang, Y. Yagi, and O. Zielke (2016), The earthquake-source inversion validation (SIV) project, *Seismol. Res. Lett.*, doi:10.1785/0220150231.

Melgar, D., W. Fan, S. Riquelme, J. Geng, C. Liang, M. Fuentes, G. Vargas, R. M. Allen, P. M. Shearer, and E. J. Fielding (2016), Slip segmentation and slow rupture to the trench during the 2015, Mw 8.3 Illapel, Chile earthquake, *Geophys. Res. Lett.*, doi:10.1002/2015GL067369, 2015GL067369.

Meng, L., J.-P. Ampuero, A. Sladen, and H. Rendon (2012), High-resolution backprojection at regional distance: Application to the Haiti M7.0 earthquake and comparisons with finite source studies, *J. Geophys. Res*, *117*(B4), doi:10.1029/2011JB008702, b04313.

Moore, G. F., N. L. Bangs, A. Taira, S. Kuramoto, E. Pangborn, and H. J. Tobin (2007), Three-dimensional splay fault geometry and implications for tsunami generation, *Science*, *318*(5853), 1128–1131, doi:10.1126/science.1147195.

Mori, J., W. D. Mooney, Afnimar, S. Kurniawan, A. I. Anaya, and S. Widiyantoro (2007), The 17 July 2006 tsunami earthquake in west Java, Indonesia, *Seismol. Res. Lett.*, *78*(2), 201–207, doi:10.1785/gssrl.78.2.201.

Newman, A. V., and E. A. Okal (1998), Teleseismic estimates of radiated

seismic energy: The E/M0 discriminant for tsunami earthquakes, *J. Geophys. Res.*, *103*(B11), 26,885–26,898, doi:10.1029/98JB02236.

Nissen, E., J. Elliott, R. Sloan, T. Craig, G. Funning, A. Hutko, B. Parsons, and T. Wright (2016), Limitations of rupture forecasting exposed by instantaneously triggered earthquake doublet, *Nature Geosci.* **9**, 330–336.

Okuwaki, R., Y. Yagi, and S. Hirano (2014), Relationship between high-frequency radiation and asperity ruptures, revealed by hybrid back-projection with a non-planar fault model, *Sci. Rep.*, *4*.

Plafker, G. (1969), Tectonics of the March 27, 1964, Alaska earthquake: Chapter I in the Alaska earthquake, March 27, 1964: regional effects, *Tech. rep.*, US Government Printing Office.

Plafker, G. (1972), Alaskan earthquake of 1964 and Chilean earthquake of 1960: Implications for arc tectonics, *J. Geophys. Res.*, *77*(5), 901–925, doi:10.1029/JB077i005p00901.

Planert, L., H. Kopp, E. Lueschen, C. Mueller, E. R. Flueh, A. Shulgin, Y. Djajadihardja, and A. Krabbenhoeft (2010), Lower plate structure and upper plate deformational segmentation at the Sunda-Banda arc transition, indonesia, *J. geophys. Res.115*(B8), doi:10.1029/2009JB006713, b08107.

Rost, S., and C. Thomas (2002), Array seismology: Methods and applications, *Rev. Geophys.*, *40*(3), 2–1–2–27, doi:10.1029/2000RG000100, 1008.

Sandwell, D. T., R. D. Müller, W. H. F. Smith, E. Garcia, and R. Francis (2014), New global marine gravity model from Cryosat-2 and Jason-

548 1 reveals buried tectonic structure, *Science*, *346*(6205), 65–67, doi:
549 10.1126/science.1258213.

550 Satriano, C., E. Kiraly, P. Bernard, and J.-P. Vilotte (2012), The 2012 Mw
551 8.6 Sumatra earthquake: Evidence of westward sequential seismic rup-
552 tures associated to the reactivation of a N-S ocean fabric, *Geophys. Res.*
553 *Lett.39*(15), doi:10.1029/2012GL052387, l15302.

554 Shao, G., X. Li, C. Ji, and T. Maeda (2011), Focal mechanism and slip history
555 of the 2011 Mw 9.1 off the Pacific coast of Tohoku earthquake, constrained
556 with teleseismic body and surface waves, *Earth, Planets, Space*, *63*(7), 9,
557 doi:10.5047/eps.2011.06.028.

558 Shulgin, A., H. Kopp, C. Mueller, L. Planert, E. Lueschen, E. R. Flueh, and
559 Y. Djajadihardja (2011), Structural architecture of oceanic plateau sub-
560 duction offshore eastern Java and the potential implications for geohazards,
561 *Geophys. J. Int.*, *184*(1), 12, doi:10.1111/j.1365-246X.2010.04834.x.

562 Spudich, P., and L. N. Frazer (1984), Use of ray theory to calculate high-
563 frequency radiation from earthquake sources having spatially variable rup-
564 ture velocity and stress drop, *Bull. Seismol. Soc. Am.*, *74*(6), 2061–2082.

565 Tamura, S., and S. Ide (2011), Numerical study of splay faults in subduction
566 zones: The effects of bimaterial interface and free surface, *J. geophys.*
567 *Res.116*(B10), doi:10.1029/2011JB008283, b10309.

568 Tregoning, P., F. K. Brunner, Y. Bock, S. S. O. Puntodewo, R. McCaffrey,
569 J. F. Genrich, E. Calais, J. Rais, and C. Subarya (1994), First geode-

570 tic measurement of convergence across the Java trench, *Geophys. Res.*
571 *Lett.21*(19), 2135–2138, doi:10.1029/94GL01856.

572 Tsai, V. C., J.-P. Ampuero, H. Kanamori, and D. J. Stevenson (2013), Esti-
573 mating the effect of earth elasticity and variable water density on tsunami
574 speeds, *Geophys. Res. Lett.*, *40*(3), 492–496, doi:10.1002/grl.50147.

575 Waldhauser, F., D. P. Schaff, T. Diehl, and E. R. Engdahl (2012), Splay faults
576 imaged by fluid-driven aftershocks of the 2004 Mw 9.2 Sumatra-Andaman
577 earthquake, *Geology*, *40*(3), 243–246, doi:10.1130/G32420.1.

578 Walker, K. T., M. Ishii, and P. M. Shearer (2005), Rupture details of the 28
579 March 2005 Sumatra Mw 8.6 earthquake imaged with teleseismic P waves,
580 *Geophys. Res. Lett.*, *32*(24), doi:10.1029/2005GL024395, l24303.

581 Wang, D., H. Kawakatsu, J. Mori, B. Ali, Z. Ren, and X. Shen (2016), Back-
582 projection analyses from four regional arrays for rupture over a curved dip-
583 ping fault: The Mw 7.7 24 September 2013 Pakistan earthquake, *J. Geo-*
584 *phys. Res.*, *121*(3), 1948–1961, doi:10.1002/2015JB012168, 2015JB012168.

585 Wang, K., and J. He (1999), Mechanics of low-stress forearcs:
586 Nankai and cascadia, *J. geophys. Res.104*(B7), 15,191–15,205, doi:
587 10.1029/1999JB900103.

588 Wang, K., and Y. Hu (2006), Accretionary prisms in subduction earthquake
589 cycles: The theory of dynamic Coulomb wedge, *J. geophys. Res.111*(B6),
590 doi:10.1029/2005JB004094, b06410.

591 Watada, S., S. Kusumoto, and K. Satake (2014), Traveltime delay and initial

592 phase reversal of distant tsunamis coupled with the self-gravitating elas-
593 tic earth, *J. geophys. Res.119*(5), 4287–4310, doi:10.1002/2013JB010841,
594 2013JB010841.

595 Weatherall, P., K. M. Marks, M. Jakobsson, T. Schmitt, S. Tani, J. E. Arndt,
596 M. Rovere, D. Chayes, V. Ferrini, and R. Wigley (2015), A new digital
597 bathymetric model of the world's oceans, *Earth and Space Science*, *2*(8),
598 331–345, doi:10.1002/2015EA000107, 2015EA000107.

599 Wei, S., E. Fielding, S. Leprince, A. Sladen, J.-P. Avouac, D. Helmberger,
600 E. Hauksson, R. Chu, M. Simons, K. Hudnut, et al. (2011), Superficial
601 simplicity of the 2010 El Mayor-Cucapah earthquake of Baja California in
602 Mexico, *Nature Geoscience*, *4*(9), 615–618.

603 Wendt, J., D. D. Oglesby, and E. L. Geist (2009), Tsunamis and splay
604 fault dynamics, *Geophys. Res. Lett.*, *36*(15), doi:10.1029/2009GL038295,
605 l15303.

606 Wessel, P., and W. H. Smith (1991), Free software helps map and display
607 data, *Eos Trans. AGU*, *72*(441), 445–446.

608 Wessel, P., W. H. F. Smith, R. Scharroo, J. Luis, and F. Wobbe (2013),
609 Generic Mapping Tools: Improved version released, *Eos Trans. AGU*,
610 *94*(45), 409–410, doi:10.1002/2013EO450001.

611 Xu, Y., K. D. Koper, O. Sufri, L. Zhu, and A. R. Hutko (2009), Rupture
612 imaging of the Mw 7.9 12 May 2008 Wenchuan earthquake from back
613 projection of teleseismic P waves, *Geochem. Geophys. Geosyst.*, *10*(4), doi:
614 10.1029/2008GC002335, Q04006.

615 Yagi, Y., and Y. Fukahata (2011), Introduction of uncertainty of Green's
616 function into waveform inversion for seismic source processes, *Geophys. J.*
617 *Int.*, *186*(2), 711–720, doi:10.1111/j.1365-246X.2011.05043.x.

618 Yagi, Y., A. Nakao, and A. Kasahara (2012), Smooth and rapid slip near
619 the Japan trench during the 2011 Tohoku-Oki earthquake revealed by a
620 hybrid back-projection method, *Earth Planet. Sci. Lett.*, *355-356*(0), 94–
621 101, doi:http://dx.doi.org/10.1016/j.epsl.2012.08.018.

622 Ye, L., T. Lay, H. Kanamori, and L. Rivera (2016a), Rupture characteristics
623 of major and great (Mw $\geq$ 7.0) megathrust earthquakes from 1990 to 2015:
624 1. Source parameter scaling relationships, *J. Geophys. Res.*, *121*(2), 826–
625 844, doi:10.1002/2015JB012426, 2015JB012426.

626 Ye, L., T. Lay, H. Kanamori, and L. Rivera (2016b), Rupture characteris-
627 tics of major and great (Mw $\geq$ 7.0) megathrust earthquakes from 1990
628 to 2015: 2. Depth dependence, *J. Geophys. Res.*, *121*(2), 845–863, doi:
629 10.1002/2015JB012427, 2015JB012427.

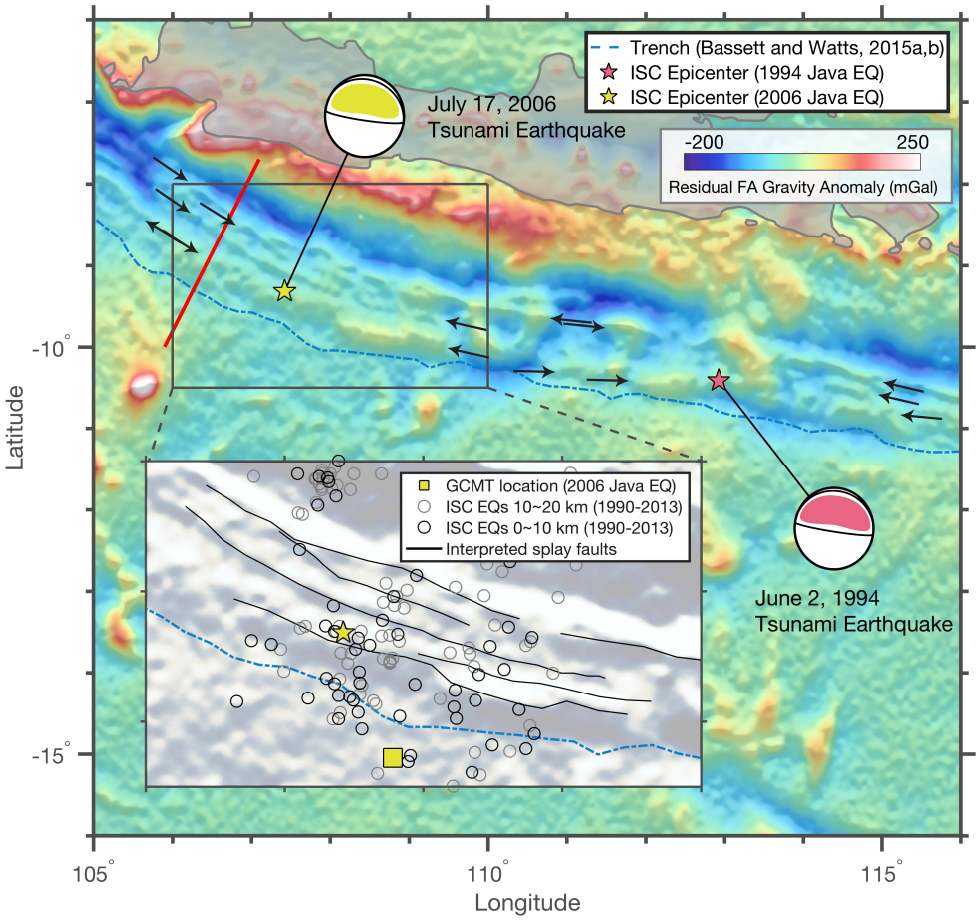

Figure 1: Residual free-air gravity anomaly, splay faults at Java subduction zone and shallow seismicity near the 2006 Java tsunami earhtquake. Black arrows show splay faults revealed by residual gravity. Insert: black circles are earthquakes (EQ) from 1993-2013 ISC catalog with M $>$ 4 and depth shallower than 10 km, gray circles are earthquakes (EQ) from 1993-2013 ISC catalog with M $>$ 4 and depth in between of 10 and 20 km (*International Seismological Centre*, 2013). Black lines are the interpreted fault traces from the residual gravity anomaly in this study. Red line is coincident seismic reflection and refraction profile SO137-03/SO138-05, which resolved steep dipping splay faults and correlates with the delineated residual gravity anomaly. Trench-axis is from *Bassett and Watts* (2015a,b).

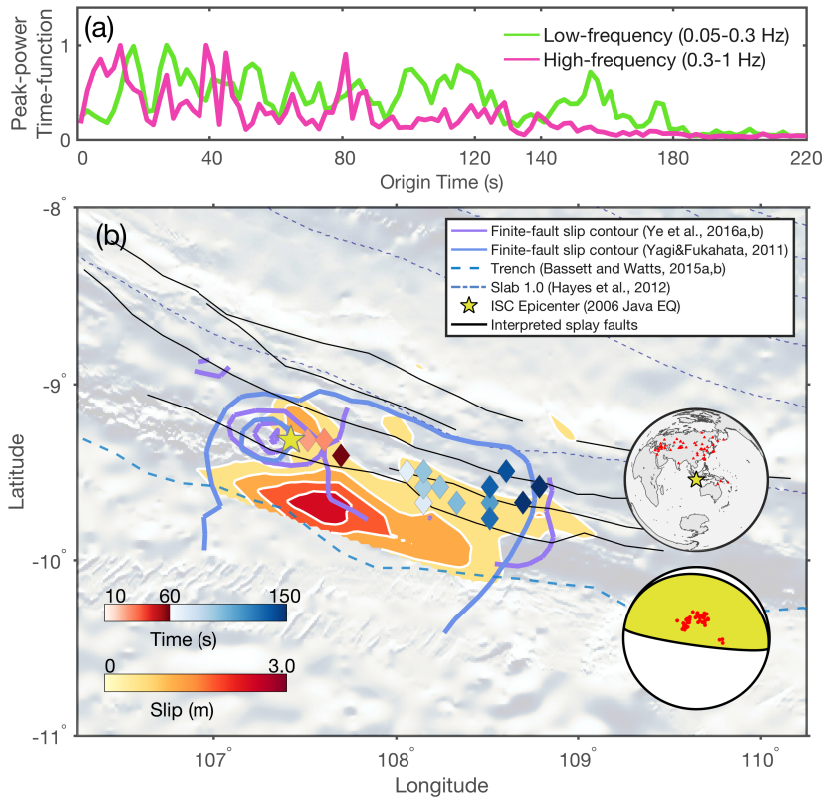

Figure 2: Seismic back-projection and tsunami back-propagation results and finite-fault slip models of the 2006 Java earthquake. (a), Peak-power time functions of two frequency bands. Peak-power time functions are self-normalized. (b), Finite-slip model obtained with both body and surface waves are the filled contours from USGS, NEIC. Finite-slip model from *Ye et al.* (2016a,b) is contoured from 0.5 to 4.5 m with 2 m separation, finite-slip model from *Yagi and Fukahata* (2011) is contoured from 0.5 to 2.5 m with 1 m separation. Diamonds show the peak-energy locations of high-frequency back-projection with 20 s averaging window and 1 s time increment. Stations used for back-projection and their P-wave polarity with the GCMT focal-mechanism are shown as inserts. The subduction geometry is from Slab 1.0 with 20 km separation (*Hayes et al.*, 2012).

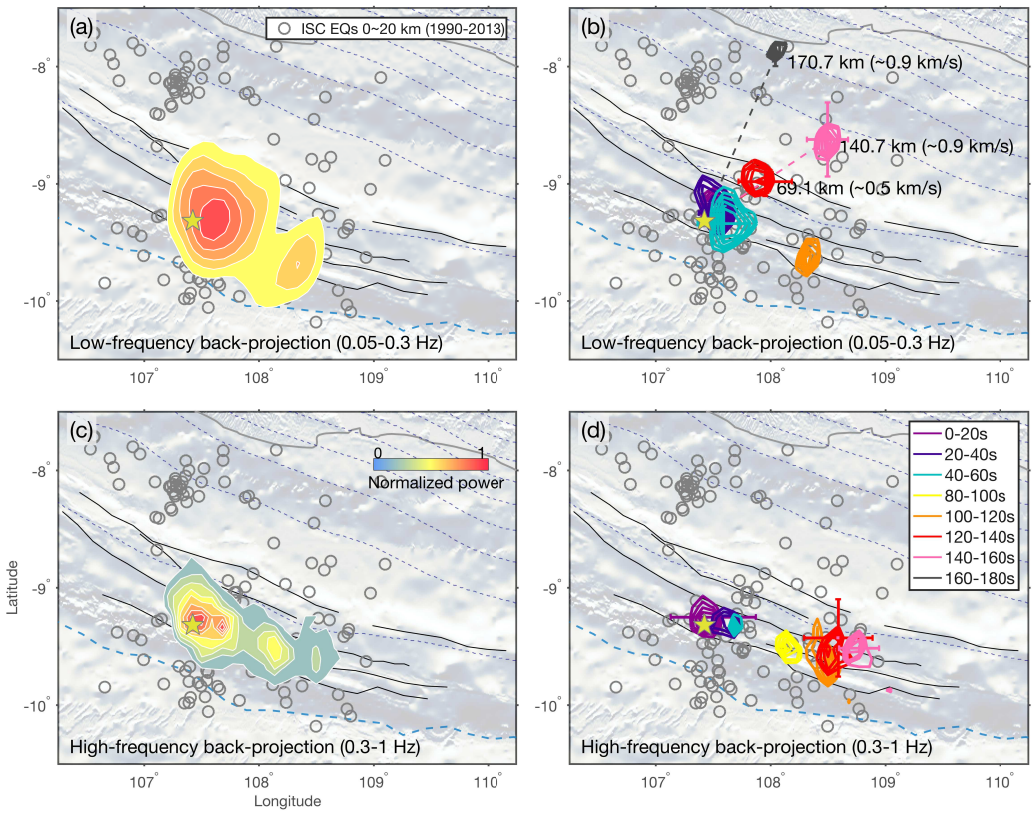

Figure 3: Back-projection results. (a), (b), Low-frequency (0.05-0.3 Hz) back-projection time-integrated energy release and snapshots. (c), (d), High-frequency (0.3-1 Hz) time-integrated energy release and snapshots. The background bathymetry gradient is from *Sandwell et al.* (2014) and *Garcia et al.* (2014). Low-frequency back-projection is contoured above 50% normalized energy contours, high-frequency back-projection is contoured above 20% normalized energy contours.

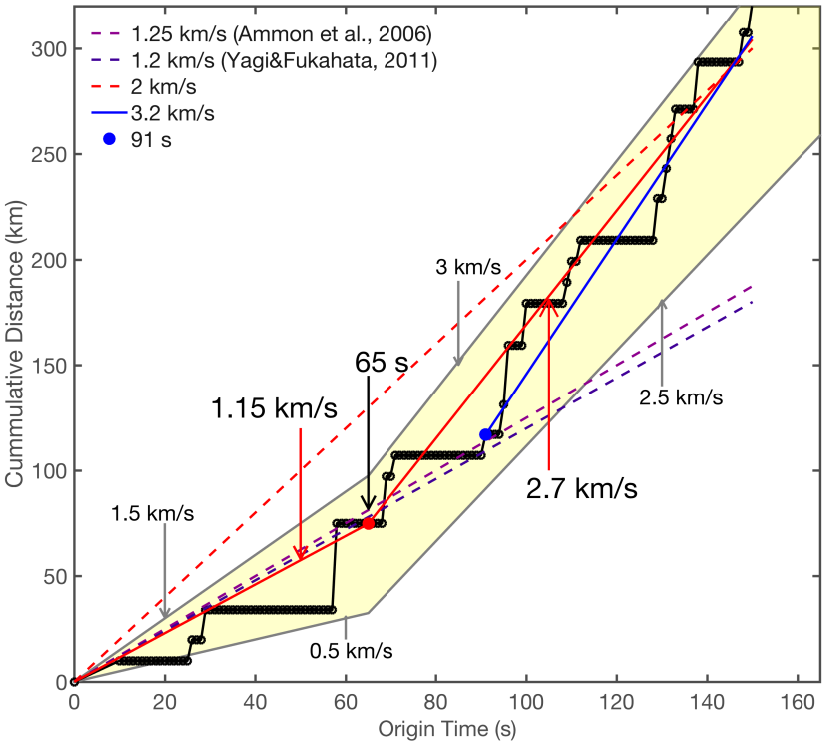

Figure 4: Cumulative distance as a function of time obtained from HF back-projection with 20 s averaging window and 1 s time increment.

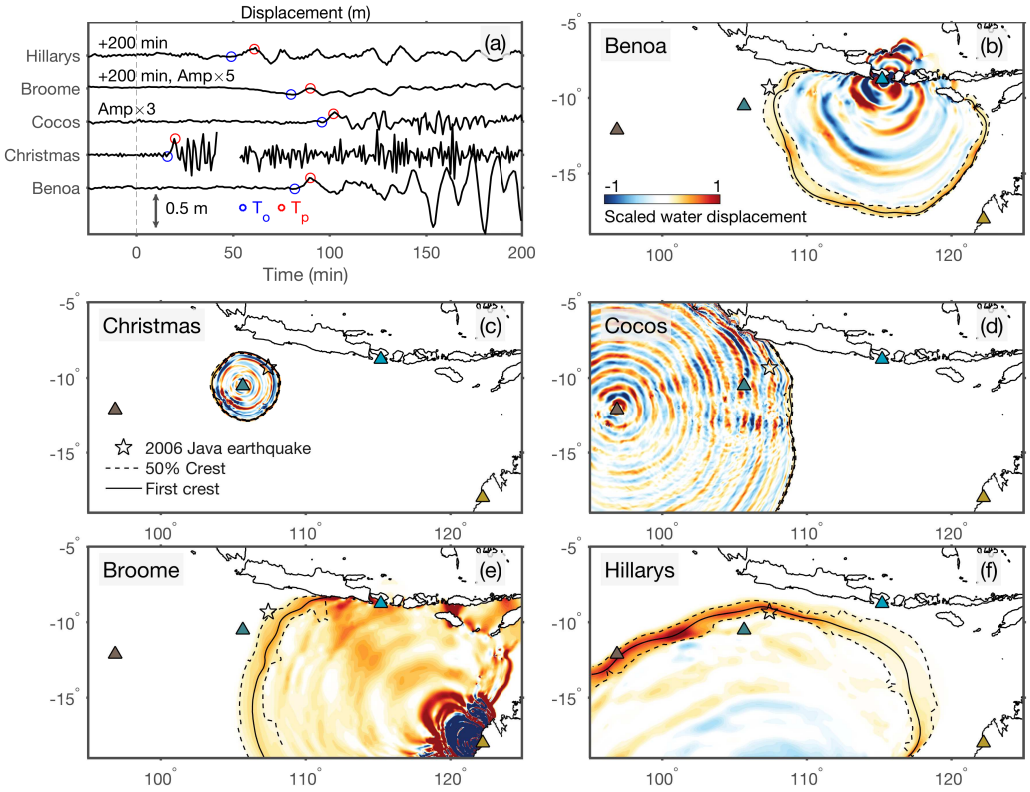

Figure 5: Tsunami back-propagation results. (a), Tsunami waveforms recorded at five tide gauges. The waveforms are high-pass filtered at 2 hours to remove tidal signals and vertically offset with amplification for two gauges for visualization purpose. The arrival time T_o (blue) and first-crest arrival time T_p (red) are marked. Hillarys and Broome records are shifted earlier by 200 min. (b)–(f), Ocean surface displacements during the back propagation of tsunami from Benoa, Christmas, Cocos, Broome, and Hillarys tide gauges (triangles). Water displacements (in color) are scaled so that the first wave front is clearly seen. The crest and outer contour (defined by 50% of the closest peak amplitude) of the first wavefront are marked by black solid and dotted lines, respectively.

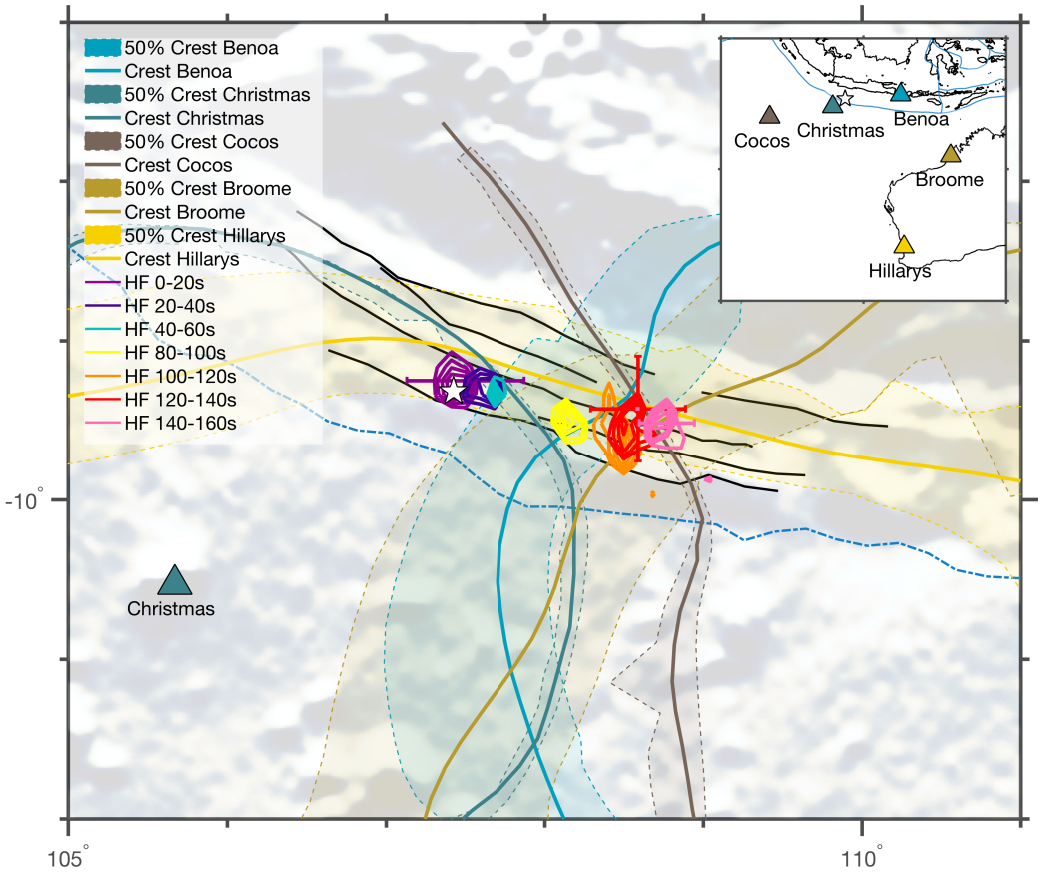

Figure 6: Tsunami wave first peak back-propagation results of five tide gauges. The solid lines show the first crest back-propagations with the shaded regions of 50% crest amplitude. Stations are shown in the insert and listed in Table 1. Colored contours are high-frequency (HF, 0.3-1 Hz) 20 s snapshots.

Table 1: Tide gauges and tsunami arrivals.

No.	Station name	Longitude (°)	Latitude (°)	T_o (min)	T_p (min)	$T_p^{'}$ (min)
1	Benoa	115.20	-8.77	82	90	89
2	Christmas	105.67	-10.53	16	20	20
3	Cocos	96.87	-12.13	96	102	101
4	Broome	122.23	-18.00	280	290	287
5	Hillarys	115.70	-31.83	249	261	258

T_o: Time of arrivals in the waveform. T_p: Time of the first peak in the waveform. $T_p^{'}$: Adjusted time used in the tsunami modeling. Benoa record is provided by the University of Hawaii Sea Level Center and the other four records by the Bureau of Meteorology, Research Centre, Australian Government.